Scalable and Disaggregated GGN Approximation Applied to a C+L+S Optical Network

Andrea D'Amico , *Graduate Student Member, IEEE*, Bruno Correia , *Graduate Student Member, IEEE*, Elliot London, *Graduate Student Member, IEEE*, Emanuele Virgillito , *Student Member, IEEE*, Giacomo Borraccini , *Graduate Student Member, IEEE*, Antonio Napoli , and Vittorio Curri , *Senior Member, IEEE*

Abstract—We investigate quality of transmission (QoT) estimation in a multi-band transmission scenario, including a wideband description of the frequency-dependent physical layer parameters and a disaggregated QoT estimation approach. In particular, we use experimentally-derived erbium- and thulium-doped fiber amplifier operational data, and simulate the generation of the nonlinear interference (NLI) noise by comparing implementations of the split-step Fourier method, the generalized Gaussian noise (GGN) model implemented in the open-source GNPy library, and an efficient approximation that provides accurate results in a limited computational time. The latter semi-analytical solution is obtained by approaching the Manakov equation from a disaggregated standpoint, including the power transfer induced by stimulated Raman scattering, along with the frequency-dependent evolution of the fiber parameters of loss, dispersion and the nonlinearity coefficient. We validate the proposed approximation within a C+L+S 400 G transmission scenario and investigate 21 channels under test that are equally spaced along the three bands.

Index Terms—Optical communications, multi-band transmission, nonlinear interference, Raman scattering, quality of transmission.

I. INTRODUCTION

OPTICAL network traffic continues to accelerate due to innovations and growth in end-user applications such as media streaming, cloud services, and the upcoming wide deployment of 5 G networking. As a result, network operators wish to increase network capacities in a financially sustainable and cost-efficient manner, preferably by maximally exploiting already-installed hardware. To achieve this goal, software-defined networking (SDN) implementations have been formulated, which provide optical infrastructures with a greater degree of flexibility, exploiting capacity dynamically and efficiently,

and permitting high levels of automation in network functions such as path computation and failure recovery. Simultaneously, the concept of open and disaggregated networking is gaining momentum, enabling operators to go beyond single-vendor frameworks and branch out into multi-vendor implementations; here, open and standardized protocols and data structures are utilized, permitting disaggregation of the optical line systems (OLSs) within the network. This framework greatly simplifies the network upgrade process, but shifts the burden of control-plane software development and maintenance to network operators, making simplification of propagation impairments and physical layer modelling a priority.

Increasing capacity with minimal capital expenditure (CAPEX) corresponds to maximizing the usage of already-deployed fiber, as new fiber deployment is typically a prohibitively expensive procedure [1]. The majority of contemporary optical networks operate within the C-band, where fiber losses are minimal, and hardware technology is mature and highly standardized. One of the most promising technologies that has been proposed to increase network capacity is multi-band/wideband transmission. Wideband transmission exploits frequencies in spectral regions beyond the C-band, presenting a potential solution to these mounting capacity demands, and has been shown to enable substantial capacity increases [2]–[4] without new fiber deployment and minimal CAPEX requirements. The first logical steps towards multi-band upgrades have already been taken with the realization of C+L-band implementations, which may more than double available network capacity when compared to single C-band architectures [5], [6]. Further steps include transmission within the S-band and beyond, with C+L+S-band systems potentially having a spectral occupancy of more than 15 THz. Unfortunately, bandwidth extensions such as these are restricted by amplifier technology and modeling capabilities, which both require further maturity within these spectral regions.

Concerning modelling, the development of simplified propagation impairment models which can be integrated into quality of transmission (QoT) tools for network planning and path computation represents a research priority. To achieve this, the two main noise sources, i.e. the amplified spontaneous emission (ASE) noise and nonlinear interference (NLI) noise must be considered separately. In an open and disaggregated networking scenario, a propagation model must firstly provide conservative

QoT estimations, in order to guarantee lightpath feasibility. For the same reason, QoT estimations must be modulation format agnostic and provide worst-case estimations, as precise knowledge of co-propagating channels may not be possible in disaggregated and multi-vendor/multi-service networking [7]. Moreover, this model must reflect a spectrally and spatially disaggregated approach, in order to enable real-time operation and reduce computational complexity. Spectral disaggregation allows a separate evaluation of the impairments that are generated by interfering channels, whereas spatial disaggregation permits a QoT estimation that is independent of the propagation history of the interfering channels and the channel under test (CUT), which may be unknown.

Creating a comprehensive and accurate physical layer model in a wideband scenario is complicated by the appearance of significant QoT impairments when bandwidths larger than the C-band are considered. Firstly, stimulated Raman scattering (SRS) effects produce an energy transfer from higher to lower frequencies, which is significant in wideband scenarios. Secondly, the physical parameters of the fiber, such as the loss coefficient and chromatic dispersion, have a dependence upon frequency that must not be overlooked. Last but not least, different spectral bands are amplified by inline amplifiers (ILAs) that depend upon different rare-earth technologies, delivering different performances in parameters such as gain, noise figure (NF), and ripple, along with introducing a non-negligible frequency dependence into the ASE noise spectral distribution, complicating the optimization of the channel input powers.

In particular, power transfer induced by the SRS is a nonlinear process, causing a tilt of the transmitted spectrum during propagation that consequently affects the power-dependent, Kerr effect-induced NLI noise generation. Approaches where the SRS efficiency function is approximated for the spectrum under investigation have been performed, permitting use of closed-form expressions for NLI modelling and providing a fast and highly accurate model for single-band scenarios [8], [9]. This simplification is no longer applicable when the transmission bandwidth exceeds the peak of the SRS spectral efficiency, which is when the CUT and the interfering channel are separated by approximately 13 THz or more. This spectral occupancy corresponds to the commercially available C+L systems which partially extend into the S-band and beyond, meaning that an alternative approach is required to ensure that a sufficient level of accuracy is achieved. In this context, the generalized Gaussian noise (GGN) model [10] is a valuable mathematical tool, as it is able to include the exact shape of the SRS function and the frequency dependence of the fiber loss coefficient, allowing an accurate wideband QoT estimation.

Within this paper we focus on wideband transmission modelling, considering both the ASE and the NLI noises. Other significant linear impairments, such as filtering penalties, are out of the scope of this work and are not considered. We explicitly derive a disaggregated redefinition of the GGN model, where the spectral content (channels) and fiber spans may be separated and considered individually in the NLI evaluation. Considering the frequency-dependent evolution of the fiber loss, α, non-linear coefficient, γ and chromatic dispersion, β, along with a numerical solution to the SRS profile, we propose a semi-analytical estimation of the NLI noise that provides accurate results in a limited computational time. The model predictions are validated with use of a simulation campaign based on the split-step Fourier method (SSFM), and compared with estimations obtained with the GGN solution implemented in the open-source GNPy library [11]. For transmission, in this work we consider three 5 THz wide spectral regions that correspond to the C-band, the L-band, and a portion of the S-band, which is denoted by S_1-band [12], defining a C+L+S_1 400 G scenario over a periodic OLS composed of 10 amplified fiber spans.

The remainder of this paper is divided as follows: in Section II we describe the multi-band system abstraction and the broader disaggregated architecture which this work may be considered under. In Section III we explain in detail the frequency-dependent physical layer parameters that are required for an adequate wideband QoT estimation and highlight any assumptions which have been made. In Section IV we provide the framework for our GGN-based, spectrally disaggregated wideband semi-analytical model. In Section V we provide details of the SSFM implementation that supports the aforementioned frequency dependent quantities and report the details of the simulation campaign performed. In Section VI we present the results of the comparison between the proposed model and the SSFM and GNPy simulations. Final comments on this study are included in Section VII.

II. MULTI-BAND AND DISAGGREGATED OPTICAL NETWORKING

A partially disaggregated optical network architecture is characterized by open and disaggregated re-configurable optical add-drop multiplexers (ROADMs) that are present at OLS ingress/egress nodes [13]. This permits wavelength division multiplexed (WDM) signals to be routed through these ROADM-to-ROADM OLSs independently [14], [15]. In this framework, optical network controllers (ONCs) are able to observe the lightpaths (LPs) that are transmitted through these OLSs and control decisions such as wavelength assignment and new LP deployment, potentially aided by an SDN implementation. Moving down to the physical layer, each OLS within this network architecture is controlled by an optical line controller (OLC), which is responsible for determining the working point of each amplifier. We investigate an OLS in this framework that permits multi-band (C+L+S_1) transmission, with each band amplified by distinct and independent amplifiers, as illustrated in Fig. 1.

To be able to assign LPs, the ONC requires a QoT estimation from the OLC, which is commonly given through the generalized signal-to-noise ratio (GSNR), expressed for each LP. The GSNR has two contributors: the optical signal-to-noise ratio (OSNR), which includes all linear contributions to the QoT degradation, including the ASE noise, and the nonlinear signal-to-noise ratio, SNR_{NL}, which includes the nonlinear impairment that is generated during fiber propagation. By considering each LP as an additive and white Gaussian noise (AWGN) channel, the
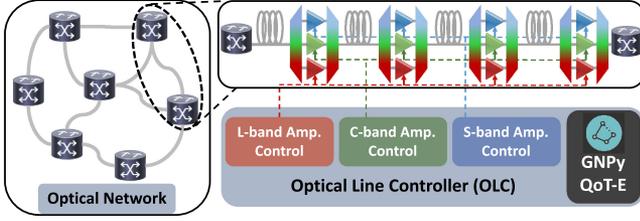
Fig. 1. The multi-band optical network architecture considered within this work. We consider an independent OLS consisting of a series of fiber spans, each followed by amplifiers providing amplification for each band, controlled by an OLC. QoT is estimated using a GNPy-based model implementation.

GSNRs for a given wavelength, λ, of each independent OLS, n, crossed by the LP can then be combined to give a total GSNR [16], [17], expressed as the inverse sum of the OSNR and SNR_{NL} contributors:

$$\text{GSNR}_{\lambda,n} = \left(\text{OSNR}_{\lambda,n}^{-1} + \text{SNR}_{\text{NL};\lambda,n}^{-1}\right)^{-1} . \tag{1}$$

After quantifying the LP QoTs using (1) it then becomes possible for the ONC to perform wavelength assignment once this information is supplied by the OLCs. In general, the working points of the amplifiers within each OLS are set by the OLCs responsible for their operation, which is managed such that the GSNR is optimal for each individual OLS [18]. In a multi-band scenario, multiple amplifiers are required for each band, each being managed separately by the amplifier controller within the OLCs, as depicted in Fig. 1. In particular, not only is maximal spectral efficiency required, but also a sufficiently uniform GSNR spectral distribution in each band under consideration. Consequently, as an optimization criterion, we select the power profile that simultaneously delivers the highest average per-band GSNR value and is sufficiently flat within the transmitted spectrum [19], [20]. This approach has the added benefit of maximizing the flexibility of LP assignment, simplifying management by the ONC at the expense of a limited reduction in spectral efficiency. Moreover, the adopted optimization procedure does not require any additional equipment, as the obtained optimal input power can be implemented by varying the booster amplifier gains (or output power) and tilt values. On the other hand, per-channel GSNR maximum optimizations have been presented in literature [21], however shaping the launch power on a per-channel basis is not always possible, as wavelength selective switches (WSSs) that are able to perform this may not be available at all amplification sites.

III. WIDEBAND PHYSICAL LAYER PARAMETERS

When implementing a wideband model it is important to ensure that the phenomenon of optical propagation is reproduced accurately and reliably, which strongly depends upon the description of the physical layer parameters. To ensure that the approach we take resembles a realistic use-case scenario, we approach the modelling of fiber and amplifier properties in two ways; by jointly utilizing experimental data retrieved by in-field measurements, and the use of theoretical models that are enhanced by commercial data-sheet information. By

convention, the full S-band is much broader than the denoted S_1-band [22], however in future realistic S-band implementations it is anticipated that a similar subdivision of this spectral region will be performed, as amplifier output power limitations prevent a single amplifier being used for the entire band. Within the following subsections we describe the essential physical layer parameters which must be considered to achieve an accurate wideband physical layer model. For further in-depth analysis of these parameters we refer the readers to [23].

A. Loss Coefficient Function

The fiber loss coefficient, α, takes into account the power loss when an optical signal propagates through a fiber. The fiber attenuation depends on the propagating signal wavelength [24], which is a result of the fiber composition and manufacturing process. From a phenomenological point of view, the contributions involved in the wavelength range between 1.2 to 1.7 μm are the Rayleigh scattering, the violent and infra-red absorption, the OH-ion absorption peaks at approximately 1.25 and 1.39 μm, and the absorption due to phosphorous within the fiber core. An effective parametric model of the loss coefficient function with respect to each phenomenological factor has been provided by [25]. With all terms in logarithmic units (dB/km), the loss coefficient profile can be expressed with respect to the optical signal wavelength, λ, as:

$$\alpha(\lambda) \simeq \alpha_{\text{S}}(\lambda) + \alpha_{\text{UV}}(\lambda) + \alpha_{\text{IR}}(\lambda)$$
$$+\alpha_{13}(\lambda) + \alpha_{12}(\lambda) + \alpha_{\text{POH}}(\lambda) , \tag{2}$$

where:

$$\alpha_{\text{S}}(\lambda) = A\lambda^{-4} + B ,$$

$$\alpha_{\text{UV}}(\lambda) = K_{\text{UV}}e^{C_{\text{UV}}/\lambda} ,$$

$$\alpha_{\text{IR}}(\lambda) = K_{\text{IR}}e^{-C_{\text{IR}}/\lambda} ,$$

$$\alpha_{13}(\lambda) = A_1 \left(\frac{A_{\text{a}}}{A_1} e^{\frac{-(\lambda-\lambda_{\text{a}})^2}{2\sigma_{\text{a}}^2}} + \frac{1}{A_1}\sum_{i=1}^{3} A_i e^{\frac{-(\lambda-\lambda_i)^2}{2\sigma_i^2}} \right) ,$$

$$\alpha_{12}(\lambda) = A_1 \left(\frac{1}{A_1}\sum_{i=4}^{5} A_i e^{\frac{-(\lambda-\lambda_i)^2}{2\sigma_i^2}} \right) ,$$

$$\alpha_{\text{POH}}(\lambda) = A_{\text{POH}}e^{\frac{-(\lambda-\lambda_{\text{POH}})^2}{2\sigma_{\text{POH}}^2}} ,$$

which represent the Rayleigh scattering, ultraviolet, infrared, OH^- and (P)OH peak absorption contributions, respectively. Focusing on a wideband scenario, the general model can be simplified by considering the relevant factors in the C-, L-, and S-bands, allowing the contributions due to the OH-ion absorption peaks at 1.25 μm and phosphorous to be neglected. Furthermore, ultraviolet absorption presents constant broadband behaviour within the band of interest. With these considerations a generic loss coefficient function may be created, considering the impact of each phenomenological contribution through the definition of four parameters; A, B, K_{IR} and A_1.

In this work, we use a loss coefficient function that has been retrieved from experimental measurements upon a standard
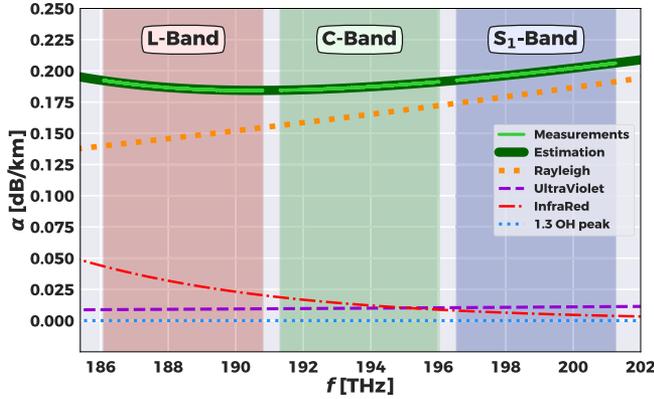
Fig. 2. The loss coefficients, α, of the fiber used within this work as a function of frequency, along with the spectral regions representing the C-, L- and S_1-bands, and the 0.5 THz guard bands between them.
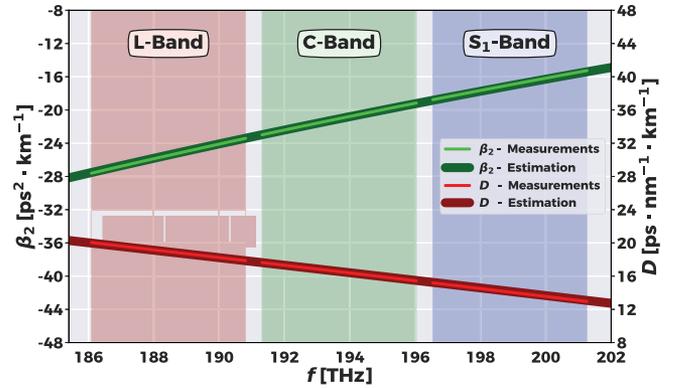

Fig. 3. The chromatic dispersion, β_2 and D parameter, of the fiber considered within this work, as a function of frequency, along with the spectral regions representing the C-, L- and S_1-bands, and the 0.5 THz guard bands between them.

single-mode fiber (SSMF). The full profile over the C+L+S_1 spectral region considered within this work is depicted in Fig. 2. By using this parametric model it is possible to separate the different contributions of each absorption phenomenon from a measured attenuation profile; we remark that this procedure has previously been performed within C-band experimental campaigns [26], [27]. Using this approach, we apply a fitting procedure to the measured loss coefficient function, using $A = 0.94\,\mathrm{dB} \cdot \mu m^4 / km$, $B = 7.03 \cdot 10^{-5}\,\mathrm{dB} / km$, $K_{\mathrm{IR}} = 5.10 \cdot 10^{11}\,\mathrm{dB} / km$, $A_1 = 3.18 \cdot 10^{-14}$, with other parameters left unchanged with respect to [25]. Furthermore, the latest generation of deployed fiber does not feature OH absorption peaks [28]; as shown in the Fig. 2, this is taken into account by our parametric model and hence we consider zero contributions due to OH absorption.

B. Chromatic Dispersion

Chromatic dispersion is the dependence of the refractive index of the medium upon the propagating optical frequency; in optical communications systems this property determines the broadening of an optical pulse propagating through the fiber, due to the different speeds of each spectral component. This phenomenon is modelled by the Taylor series expansion of the mode-propagation constant, β, with respect to the central frequency of the pulse. Using this approach, β_2 is defined as the second derivative of β with respect to the optical frequency computed in the pulse central frequency, and is the parameter that describes the pulse broadening. From an application point of view, optical fiber producers report the dispersion parameter, D, as a function of the optical pulse wavelength within fiber data sheets. Considering SSMF fiber (e. g. CorningSMF-28e), a common expression of this parameter is:

$$D(\lambda) \approx \frac{S_0}{4} \left[\lambda - \frac{\lambda_0^4}{\lambda^3} \right] , \qquad (3)$$

where S_0 is the zero dispersion slope and λ_0 is the zero dispersion wavelength. D is related to β_2 according to the following

relation:

$$\beta_2(\lambda) = -\frac{\lambda^2}{2\pi c} D , \qquad (4)$$

where c is the speed of light in a vacuum. In this study, we use the dispersion parameter profile of a SSMF fiber measured within the spectral region corresponding to the C+L+S_1 bands. We set $S_0 = 0.089\ ps / nm^2 / km$ and $\lambda_0 = 1314\ nm$, which are values within the common tolerance ranges of commercial SSMF. A graphical representation of D and the related β_2 parameters is reported in Fig. 3.

C. Nonlinear Coefficient

The fiber nonlinear contribution is mathematically weighted within the pulse propagation equation by the nonlinear coefficient, γ. Formally, it is defined in terms of optical power as:

$$\gamma(\lambda) = \frac{2\pi}{\lambda} \frac{n_2}{A_{eff}} , \qquad (5)$$

where n_2 is the nonlinear Kerr parameter and A_{eff} is the effective mode area. When the mode profile of the pulse is well approximated by a Gaussian function, the effective area can be evaluated as $A_{eff} = \pi\, w^2$, where w is the mode radius, which depends upon the central pulse wavelength and the fiber geometry. Specifically, the mode radius can be expressed as $w = a / \sqrt{\ln V}$, where a is the fiber core radius and the parameter V is the normalized frequency. This may be written in case of a small relative index step at the core-cladding interface, $\Delta \approx (n_1 - n_c) / n_1$, as:

$$V(\lambda) = \frac{2\pi}{\lambda}\, a\, n_1 \sqrt{2\Delta} , \qquad (6)$$

where n_1 is the core refractive index and n_c is the cladding refractive index.

In this work, we use a nonlinear coefficient profile and effective area curve that depends upon frequency, as shown in Fig. 4, fixing the basic manufacturing fiber parameters to common SSMF values of $a = 4.2\ \mu m$ and $n_2 = 2.6 \cdot 10^{-20}\ m^2 / W$.
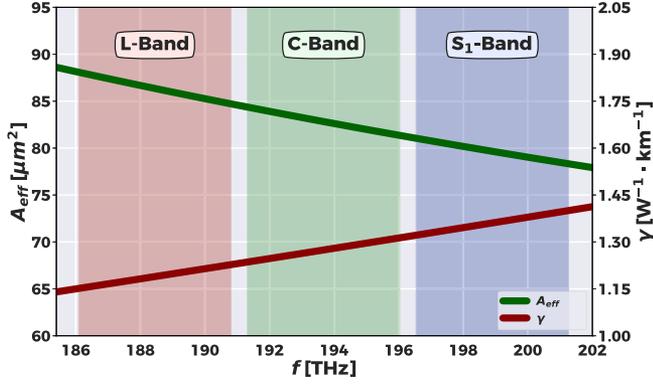
Fig. 4. The effective area, A_{eff}, and nonlinear coefficient, γ, of the fiber considered within this work as a function of frequency, along with the spectral regions representing the C-, L- and S$_1$-bands, and the 0.5 THz guard bands between them.

Fig. 5. Experimental Raman gain coefficient curve for fused silica.

Considering a step index fiber, the refractive indexes are computed assuming a cladding refractive index of 1.45 and a refractive index difference with respect to the core of 0.31%.

D. Raman Gain Coefficient

A significant broadband nonlinear phenomenon that takes place in WDM comb optical fiber propagation is the SRS [29]. The SRS involves the interaction between the propagating electromagnetic field and the dielectric medium of the fiber. In optical fiber communications, the SRS due to propagation of a WDM comb is also known as the Raman cross-talk, as the interaction in this case is only due to the different channels within the spectrum. The fundamental parameter that describes the regulation of the power transfer between channels during fiber propagation is the Raman gain coefficient, g_R, quantifying the coupling between a specific pair of channels with a frequency shift of $\Delta f = f_p - f_s$, where p and s represent the index of the channel at higher (pump) and lower (Stokes wave) frequencies, respectively. This coefficient depends on several features of the fiber and the propagating channel modes: the type and the concentration of dopants in the fiber core, the reciprocal polarization state, and the mode overlap between the pump and the Stokes wave and the absolute frequency of the pump. For a specific fiber, it is possible to measure the Raman gain coefficient profile using a reference pump at a frequency f_{ref} [30]. The resulting curve can be expressed in terms of optical power as:

$$g_0(\Delta f, f_{ref}) = \frac{\gamma_R(\Delta f, f_{ref})}{A_{eff}(\Delta f, f_{ref})} , \quad (7)$$

where γ_R is the Raman gain coefficient in terms of mode intensity (expressed in m / W) and $A_{eff}(\Delta f, f_{ref})$ is the effective area considering the overlap between the pump and the Stokes wave. The effective area can be estimated by taking the average of the effective areas at the single pump and Stokes wave frequencies, assuming a Gaussian mode intensity distribution [31].
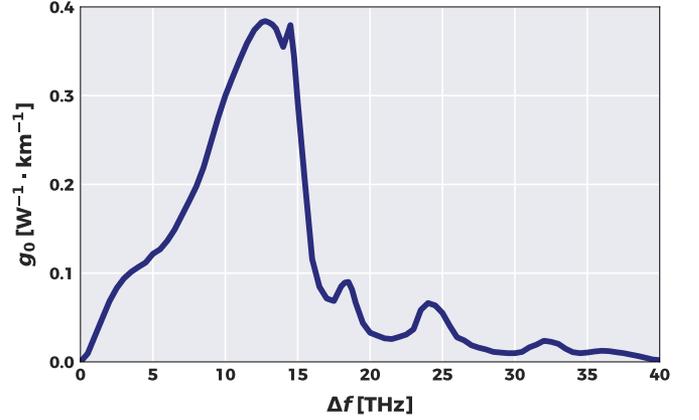
In order to comprehensively simulate optical fiber propagation and include SRS effects, the complete Raman gain coefficient can be modelled by means of the following expression:

$$g_R(\Delta f, f_p) = k_{pol}^{ps} \, g_0(\Delta f, f_{ref}) \frac{f_p}{f_{ref}} \frac{A_{eff}(\Delta f, f_{ref})}{A_{eff}(\Delta f, f_p)} , \quad (8)$$

where k_{pol}^{ps} takes into account the reciprocal polarization state between the pump and the Stokes wave, and the ratios between the frequencies and effective areas account for the scaling of the pump and effective area. Focusing on germanosilicate fibers, in particular on SSMF, the germanium concentration within the core fiber is extremely low, producing a refractive index difference of a fraction of a percentage point. In this work, we use an experimental Raman gain coefficient curve that corresponds to that of the fused silica reported in Fig. 5, characterized by the double peak at approximately 13 THz. In the simulation model, we assume that all propagating channels within the WDM comb are depolarized, introducing a unitary polarization coefficient k_{pol}. Furthermore, since no Raman amplification is present within the considered use case, we neglect the scaling of the pump reference frequency and the effective area.

E. Amplification Parameters

As briefly described in Section II and shown in Fig. 1, in a multi-band scenario each set of channels within a spectral band is amplified by a distinct device. In this work, we have utilized two erbium-doped fiber amplifiers (EDFAs) for C- and L-bands, respectively. Instead, S$_1$-band amplification is performed by thulium-doped fiber amplifiers (TDFAs) [32]. The usage of different amplifiers for each set of channels comes from the fact that EDFAs, despite being a more mature technology than TDFAs, do not perform well for spectral regions outside of the C- and L-bands. Moreover, output power limitations of current amplifiers do not permit usage of an unlimited number of channels, which requires the L- and C-bands being amplified by distinct EDFAs, with two TDFAs also predicted to be required for full S-band amplification. Another possibility is the usage of Raman amplification applied to multi-band transmission, which can provide an ultra-wide gain profile [33] and the potential to also control the mean gain and tilt [34]. The usage of Raman
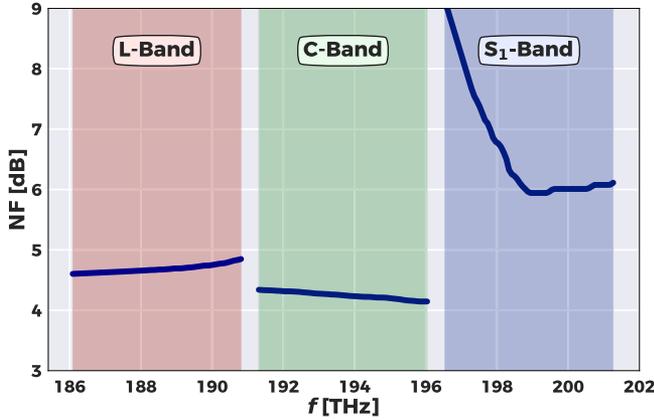
Fig. 6. The noise figures, NF, of the model EDFAs (C- and L-bands) and TDFA (S_1-band) used within this work as a function of frequency, along with the spectral regions representing the C-, L- and S_1-bands, and the 0.5 THz guard bands between them.

amplification is out of the scope of this work and we carry our analyses using only EDFA/TDFA amplification.

The two amplifier parameters used to properly model an OLS performance are the gain and NF, which determines the ASE noise and the signal propagation. The target gain, or output power, is determined by the OLC for all amplifiers within an OLS. Usually, the gain profile has fluctuations/ripples [35] that should be considered in the model. In this work, we assume an ideal amplifier which can recover the optimal launch power profile. In general, the NF varies with the amplifier gain values, and this phenomenon can be incorporated to the input power optimization procedure described in Sec II. Nevertheless, in this work, we consider the frequency-dependent NF profiles shown in Fig. 6 for each spectral band, which have been measured on commercial amplifier at a fixed gain level.

IV. SCALABLE AND DISAGGREGATED APPROXIMATE MODEL

Bearing in mind the disaggregated network framework, without any loss of generality, we focus our investigation on a multi-band C+L+S_1 transmission scenario for a given OLS. (1) can be further disaggregated on a span-by-span basis, where both the $\text{OSNR}_{\lambda,n}$ and $\text{SNR}_{NL;\lambda,n}$ of the n-th OLS can be expressed as follows:

$$\text{OSNR}_{\lambda,n} = \left(\sum_{s=1}^{N_s} \frac{P_{\text{ASE};\lambda}^{(s)}}{P_\lambda^{(s)}} \right)^{-1} = \frac{1}{N_s} \frac{P_\lambda}{P_{\text{ASE};\lambda}}, \qquad (9)$$

$$\text{SNR}_{\text{NL};\lambda,n} \leq \left(\sum_{s=1}^{N_s} \frac{P_{\text{NLI},\lambda}^{(s)}}{P_\lambda^{(s)}} \right)^{-1} = \frac{1}{N_s} \frac{P_\lambda}{P_{\text{NLI};\lambda}}, \qquad (10)$$

where N_s is the OLS number of fiber spans, $P_\lambda^{(s)}$, $P_{\text{ASE};\lambda}^{(s)}$ and $P_{\text{NLI};\lambda}^{(s)}$ are, respectively, the signal, ASE noise and NLI noise powers at the s-th span termination (in this work, each span is defined as a fiber followed by an EDFA) for a given λ. In this

investigation, we focus on a periodic OLS, as the disaggregation paradigm allows a straightforward generalization of this scenario. Consequently, we obtain the right-hand side expressions in both (9) and (10), defining $P_\lambda = P_\lambda^{(s)}$, $P_{\text{ASE};\lambda} = P_{\text{ASE};\lambda}^{(s)}$, $P_{\text{NLI};\lambda} = P_{\text{NLI};\lambda}^{(s)} \; \forall s \in [1, N_s]$. (9) is verified with a high level of accuracy for a wide set of realistic optical systems, whereas the equality in (10) is verified only when there is no correlation between the NLI noise generated in each distinct fiber span. The latter condition is not fulfilled in a real transmission scenario and, as shown in [36], [37], this is due to the single-channel (SC) component of the NLI noise that accumulates coherently span-by-span. In general, (10) provides a non conservative estimation of the accumulated NLI noise, which can lead to a reduction of the expected margin or, in the worst case, an out of service scenario. As proposed in [38], this effect can be managed effectively by separating the NLI noise generated in each fiber span into its SC, $P_{\text{SC};\lambda}$, and cross-channel (XC), $P_{\text{XC};\lambda}$, contributions and including an asymptotic coefficient, C_∞, that takes into account the coherent SC accumulation. As observed in [36], [37], the four-wave-mixing (FWM) contribution to the NLI noise can be neglected without any significant loss in model accuracy for standard optical system transmissions. Even if the number of FWM contributions increase exponentially with the number of interfering channels, the overall FWM contribution to the NLI noise can be neglected also in a multi-band transmission scenario, as the entire inter-band NLI effect is negligible as shown in [19] for a C+L transmission scenario, roughly 10 THz of spectrum bandwidth. By means of the asymptotic overestimation, a conservative estimation of the NLI noise power, $P_{\text{NLI};\lambda}$, can be substituted in (10) obtaining the following expression:

$$\text{SNR}_{\text{NL};\lambda,n} > \frac{1}{N_s} \frac{P_\lambda}{[(1 + C_\infty) P_{\text{SC};\lambda} + P_{\text{XC};\lambda}]}. \qquad (11)$$

Given this span-by-span disaggregation, the analysis of the signal degradations introduced by each OLS can be reduced to the investigation of the single span effects.

When the EDFA parameters are known and the spectral load is constant, the single span ASE noise can be calculated with the following formula:

$$P_{\text{ASE},\lambda} = h f_\lambda \text{NF}(f_\lambda)(G(f_\lambda) - 1) R_{s_\lambda}, \qquad (12)$$

where f_λ is the central frequency of the channel corresponding to λ, $\text{NF}(f_\lambda)$ and $G(f_\lambda)$ are the NF and gain evaluated at the channel central frequency, respectively, and R_{s_λ} is the channel symbol rate. When EDFA parameters are unknown or inaccurate, and/or the spectral load is not constant, additional information is required in order to properly model and simulate the ASE noise power profile. In these scenarios, telemetry and monitoring data can be used to overcome the lack of information, e.g. with machine learning frameworks [26], [39], or with a model based characterization as in [27].

Regarding the NLI noise, a significant level of complexity remains in modeling and simulation, even when the fiber physical parameters described in Section III are accurately known. Valuable models have been proposed in order to estimate the NLI noise generation including the SRS [8]–[10].

These models have been accurately validated in different scenarios, both with simulations and experiments. Nevertheless, a satisfactory level of accuracy is not guaranteed, and likely compromised in a wideband scenario. The objective of this analysis is to obtain a wideband extended model that includes the frequency-dependent variations of all physical layer parameters described in Section III, that also maximally enables spectral disaggregation (a fully disaggregated model is prevented by the nonlinear nature of the investigated phenomena). As described in Section II, the disaggregated approach enables the most dynamic, flexible and efficient system optimization and operation. Moreover, as per the span-by-span accumulation, spectral disaggregation allows the distinct, simultaneous effects that contribute to the NLI noise generation to be separated.

Consequently, we wish to define a spectrally disaggregated version of the GGN NLI power spectral density, as expressed in (2) in [10]. We choose this model as the solution of the SRS equations is not approximated, which enables further investigations into larger bandwidths. Additionally, a spectrally separated implementation of the GGN is already present in GNPy, and has been validated in several experimental test-beds, both in laboratories and brown-field infrastructures [18], [40], [41]. However, this spectrally separated GGN implementation is not explicitly disaggregated and does not take into account the frequency-dependent variations of the fiber physical parameters.

In order to obtain a disaggregated model where all frequency-dependent variations are properly considered, we first analyze the dual-polarization Manakov equation [42]:

$$\partial_z \vec{A}(z,t) = \left(-\hat{\alpha}(z) + \iota\hat{\beta}\right)\vec{A}(z,t)$$
$$- \iota\frac{8}{9}\hat{\gamma}\left[\vec{A}(z,t) \cdot \vec{A}^*(z,t)\right]\vec{A}(z,t), \quad (13)$$

where $\vec{A}(z,t)$ is the dual-polarization modal amplitude at the position z at the time t; $\hat{\alpha}(z)$, $\hat{\beta}$ and $\hat{\gamma}$ are the gain/loss, dispersion and nonlinear coefficient operators, respectively; ι represents the imaginary unit, and the operator $\cdot$ is the standard product in the bi-dimensional polarization space. In particular, the gain/loss, dispersion and nonlinear coefficient are defined as operators in the time domain, as they are frequency-dependent. Furthermore, the gain/loss coefficient operator encompasses the power variation along the position induced by both the fiber loss and the SRS.

The Manakov equation significantly simplifies NLI estimation by neglecting the polarization mode dispersion (PMD) introduced by the fiber propagation. A more general approach can be obtained considering the dual-polarization coupled nonlinear Schrodinger equation (DP-CNLSE) [42], which takes into account the stochastic birefringence realization inducing the PMD. Nevertheless, in this study we focus on a solution in a disaggregated network framework, where the signal transmitted through a specific OLS can be considered as fully Gaussian and depolarized, for each span. Under these conditions, it has been shown that the effect of PMD on the NLI generation is negligible [43], and that the small differences between the solutions of the Manakov equation and the DP-CNLSE do not

vary significantly when enlarging the investigated bandwidth up to 4 THz. In this analysis we assume that the solutions of the Manakov equation and the DP-CNLSE are not significantly different when the C+L+S$_1$-band transmission scenario is considered, as their differences do not depend on the overall bandwidth.

The formal solution of (13) is a combination of a linear, $\mathcal{L}(z)$, and a nonlinear, $\mathcal{N}(z)$, operators applied to the modal amplitude at the fiber input, $\vec{A}(z=0,t) = \vec{A}(t)$:

$$\vec{A}(z,t) = \mathcal{L}(z)\mathcal{N}(z)\vec{A}(t), \quad (14)$$

given the following properties:

$$\partial_z\mathcal{L}(z)\mathcal{L}^{-1}(z) = \left(-\hat{\alpha}(z) + \iota\hat{\beta}\right), \quad (15)$$

$$\mathcal{L}(z)\partial_z\mathcal{N}(z)\mathcal{N}^{-1}(z)\mathcal{L}^{-1}(z) = -\iota\frac{8}{9}\hat{\gamma}\left[\vec{A}(z,t) \cdot \vec{A}^*(z,t)\right]. \quad (16)$$

In standard fiber-optic transmission the nonlinear term in (13) can be considered as a perturbation source of the NLI noise, $\vec{N}(z,t)$, of the linear propagation of the signal, $\vec{A}_{\mathrm{L}}(z,t) = \mathcal{L}(z)\vec{A}(t)$:

$$\vec{A}(z,t) \approx \vec{A}_{\mathrm{L}}(z,t) + \mathcal{L}(z)\vec{N}(z,t), \quad (17)$$

where $\vec{N}(z,t)$ includes the perturbative expansion of $\mathcal{N}(z)$ up to a certain γ order, and (17) is an identity only when all perturbation orders are summed to obtain $\vec{N}(z,t)$. In optical communications scenarios, an accurate estimation of the NLI can be obtained by considering the first order perturbation in γ of $\mathcal{N}(z)$, and the noise field can be calculated as the solution of the following differential equation:

$$\mathcal{L}(z)\partial_z\vec{N}(z,t) = -\iota\frac{8}{9}\hat{\gamma}\left[\vec{A}_{\mathrm{L}}(z,t) \cdot \vec{A}_{\mathrm{L}}^*(z,t)\right]\vec{A}_{\mathrm{L}}(z,t). \quad (18)$$

More precisely, $\mathcal{L}(z)$ is not a linear operator in general as $\tilde{\alpha}(z)$ depends on the $\vec{A}(z,t)$ power due to the SRS. Nevertheless, when the perturbative approach is considered, the SRS effect can be solved separately and $\mathcal{L}(z)$ can be treated as a linear operator. In general, $\vec{A}(z,t)$ is the superposition of N_{ch} uncorrelated signals and can be written as follows:

$$\vec{A}(z,t) = \sum_{i=1}^{N_{ch}}\vec{A}_{\lambda_i}(z,t) = \sum_{i=1}^{N_{ch}}\int_{-\infty}^{\infty}\mathrm{d}f\vec{A}_{\lambda_i}(z,f)e^{\iota 2\pi ft}, \quad (19)$$

where $\vec{A}_{\lambda_i}(z,f_i)$ is the Fourier transformation of $\vec{A}_{\lambda_i}(z,t)$. In the frequency domain, the $\mathcal{L}(z)$ is diagonal and has the following solution for the ith channel:

$$\vec{A}_{\mathrm{L},\lambda}(z,f) = \sqrt{\frac{P_\lambda}{2R_{s_\lambda}}\rho_\lambda(z)}\,e^{-\iota\beta(f)z}\,\vec{\varphi}_\lambda(f), \quad (20)$$

where P_λ is the total channel power over the two polarization states, R_{s_λ} is the channel symbol rate, $\rho_i(z)$ is the channel power gain/loss profile along z, and $\vec{\varphi}_i(f_i)$ is the channel transmitted signal, $\vec{A}_i(f)$, in the frequency domain, normalized with respect to both the average channel power for each polarization and the channel symbol rate. In particular, $\rho_\lambda(z)$ can be found for each

channel by solving the coupled SRS equations [31]:

$$
\begin{aligned}
\frac{\mathrm{d}P_{\lambda_i}(z)}{\mathrm{d}z} =&\ -2\hat{\alpha}(z)P_{\lambda_i}(z) \\
=&\ -\alpha_{\lambda_i}P_{\lambda_i}(z) \\
&- \sum_{f_{\lambda_j} < f_{\lambda_i}} \frac{f_{\lambda_j}}{f_{\lambda_i}} g_R\left(|f_{\lambda_i} - f_{\lambda_j}|\right) P_{\lambda_i}(z)P_{\lambda_j}(z) \\
&+ \sum_{f_j > f_i} g_R\left(|f_{\lambda_i} - f_{\lambda_j}|\right) P_{\lambda_i}(z)P_{\lambda_j}(z),
\end{aligned}
\quad (21)
$$

where $P_{\lambda_i}(z) = P_{\lambda_i}\rho_{\lambda_i}(z)$; α_{λ_i} and $g_R(|f_{\lambda_i} - f_{\lambda_j}|)$ are obtained from (2) and (7), respectively, assuming these values are constant within the channel bandwidth. This set of coupled equations can be solved numerically by evaluating the power profile for all channels incrementally by position [44]. This procedure provides an accurate result if the position increments are small enough, and has been used within this work and implemented in GNPy.

In general, we can define the metric $P_{\mathrm{NLI};\lambda}$ used in (10) as the noise variance evaluated when a specific channel, λ, is received. In further detail, in order to estimate $P_{\mathrm{NLI};\lambda}$, we suppose that the channel signals are received after propagation through the fiber span with an ideal transceiver that applies the matched filter for the λ channel, compensates for all accumulated dispersion and PMD, and equalizes the channel signal by compensating for the entire fiber gain/loss profile. By means of these transformations, the channel signal reduces to $\vec{\varphi}_\lambda(f_\lambda) + \vec{N}_\lambda(f)$, where L_s is the span length and $\vec{N}_\lambda(f) = \vec{N}_\lambda(z = L_s, f)$ is the solution of (18) in the frequency domain. At this point, the ideal receiver can sample the signal and the $P_{\mathrm{NLI};\lambda}$ can be defined as the variance of the $\vec{N}_\lambda(f)$ power over all symbol sequences in the realization space:

$$
P_{\mathrm{NLI};\lambda} = \int_{-\infty}^{\infty} \mathrm{d}f \int_{-\infty}^{\infty} \mathrm{d}f'\ \mathbf{Cov}\left[\vec{N}\right],
$$

$$
\mathbf{Cov}\left[\vec{N}\right] = \left\langle \vec{N}_\lambda^*(f') \cdot \vec{N}_\lambda(f) \right\rangle - \left\langle \vec{N}_\lambda^*(f') \right\rangle \cdot \left\langle \vec{N}_\lambda(f) \right\rangle, \quad (22)
$$

where $\langle \cdots \rangle$ represents the expectation value operator over the considered ensemble. As each normalized transmitted channel signal, $\vec{\varphi}_\lambda(f)$, can be considered as Gaussian distributed (in the symbol sequence realization space), with a unitary power on each polarization, and statistically independent with respect to other channels, the expectation value operator verifies the following property:

$$
\left\langle \prod_{i,j}^{N} \vec{\varphi}_{\lambda_i}^*(f_i) \cdot \vec{\varphi}_{\lambda_j}(f_j) \right\rangle = \sum_{p \in \mathbf{P}} \prod_{i,j}^{N} \left\langle \vec{\varphi}_{\lambda_i}^*(f_i) \cdot \vec{\varphi}_{\lambda_j}(f_j) \right\rangle
$$

$$
= \sum_{p \in \mathbf{P}} \prod_{i,j}^{N} 2\delta_{\lambda_j}^{\lambda_i}\delta(f_i - f_j), \quad (23)
$$

where $\mathbf{P}$ is the space of all i, j permutations that results in a nonzero expectation value, $\delta_{\lambda_j}^{\lambda_i}$ and $\delta(f_i - f_j)$ are the Kronecker and Dirac deltas, respectively.

With a few steps of algebra, as in [10], the solution of (18) can be evaluated in (22) and, separating the $P_{\mathrm{SC},\lambda}$ and $P_{\mathrm{XC},\lambda}$ terms, we obtain:

$$
P_{\mathrm{SC},\lambda} = \eta_{\lambda,\lambda}P_\lambda^3 = \gamma_\lambda^2 \mathcal{W}_{\mathrm{SC}}\mathcal{I}_\lambda^\lambda(L_s)\frac{P_\lambda^3}{Rs_\lambda{}^3}, \quad (24)
$$

$$
P_{\mathrm{XC},\lambda,\kappa} = \eta_{\lambda,\kappa}P_\lambda P_\kappa^2 = \gamma_\lambda^2 \mathcal{W}_{\mathrm{XC}}\mathcal{I}_\kappa^\lambda(L_s)\frac{P_\lambda}{Rs_\lambda}\left(\frac{P_\kappa}{Rs_\kappa}\right)^2, \quad (25)
$$

where λ and κ represent the CUT and the interfering channel, respectively. Additionally:

$$
\mathcal{W}_{\mathrm{SC}} = (1 + C_\infty)\left(\frac{8}{9}\right)^2 \frac{6}{2^3} = (1 + C_\infty)\frac{16}{27},
$$

$$
\mathcal{W}_{\mathrm{XC}} = 2\frac{16}{27},
$$

are the SC and XC weights coming from the statistics and the polarization, whereas

$$
\mathcal{I}_\kappa^\lambda(L_s) = \int_{-\infty}^{\infty}\mathrm{d}f \int_{-\infty}^{\infty}\mathrm{d}f' \int_{-\infty}^{\infty}\mathrm{d}f'' \mathrm{I}_\kappa(f')\mathrm{I}_\kappa(f' - f'')
$$

$$
\cdot\ \mathrm{I}_\lambda(f - f'')\mathrm{I}_\lambda(f)\left|\Psi_\kappa\left(L_s; f', f'', f\right)\right|^2, \quad (26)
$$

where:

$$
\mathrm{I}_\lambda(x) = \begin{cases} 1 & \text{if } x \in \mathrm{I}_\lambda \equiv \left[f_\lambda - \frac{R_{s_\lambda}}{2}, f_\lambda + \frac{R_{s_\lambda}}{2}\right], \\ 0 & \text{otherwise} \end{cases}
$$

$$
\Psi_\kappa\left(L_s; f', f'', f\right) = \int_0^{L_s}\mathrm{d}z\ \rho_\kappa^2(z')e^{\iota 2\pi^2 \Delta\beta_\kappa^\lambda(f', f'', f)z},
$$

$$
\Delta\beta_\kappa^\lambda(f', f'', f) = \beta(f') - \beta(f' - f'') + \beta(f - f'') - \beta(f)
$$

$$
\approx \frac{(2\pi)^2}{2}f''(f' - f)\left[\beta_2(f') + \beta_2(f)\right]. \quad (27)
$$

In general, further analytical simplifications of (26) may be possible, but (27) cannot be analytically integrated, as $\rho_\kappa^2(z)$ is evaluated numerically and its exact value depends on the signal launch power. As we have obtained a disaggregated version of the GGN that allows a more accurate depiction of the multi-band scenario (as presented in [10]), we focus on finding a numerical approximation to (26) that allows a fast and accurate simulation of the investigated C+L+S$_1$ transmission scenario.

The GGN implementation in GNPy evaluates (26) by numerical integration with a less precise expression of the frequency-dependent fiber parameters. This solution is time consuming, does not scale properly with the number of the interfering channels, and it is prone to numerical errors due to artificial resonances, especially when the interference channel is spectrally distant from the CUT. In this work, we derive a numerical solution to (26) through an approximation: first we divide the fiber length in N uniform steps, $\{z_0 = 0, \ldots, z_m = m\Delta z, \ldots, z_N = L_s\}$, such that within each step $\rho_{\kappa,m}^2(z) = \rho_{\kappa,m}^2(z_m)e^{-\hat{\alpha}_m(z - z_m)}$. By means of this decomposition, (27) can be solved incrementally by applying an analogous methodology to the one reported in [45], providing the following
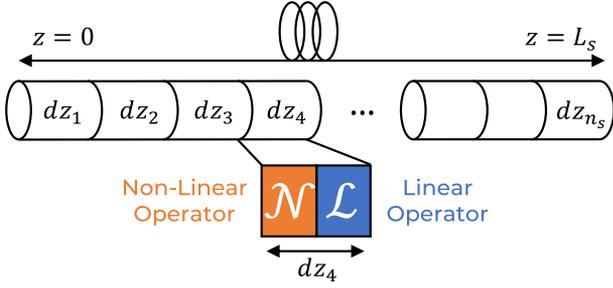
Fig. 7. Scheme of the split-step Fourier method. The linear, L, and non-linear, N, operators are applied separately in each dz step.

Fig. 8. Gain-Loss profile depending on SRS and frequency-dependent fiber loss.

approximate solution on the m-th step:

$$\Psi_\kappa\left(z_m; f,' f,'' f\right) \approx \frac{L_{eff}(z_m)}{\left[1 - \iota \frac{\Delta \beta_\kappa^\lambda(f,'f,''f)}{\tilde{\alpha}_m}\right]} . \quad (28)$$

where the effective length on each step, $L_{eff}(z_m)$ is defined as $L_{eff}(z_m) = [\rho_{\kappa,m}^2(z_m) - \rho_{\kappa,m}^2(z_{m+1})]/\tilde{\alpha}_m$. Finally, by substituting this approximated solution into (26) we obtain:

$$\mathcal{I}_\kappa^\lambda(L_s) \approx \sum_{m,n} \frac{\sqrt{|\tilde{\alpha}_m \tilde{\alpha}_n|} L_{eff}(z_m) L_{eff}(z_n) R_{s_\lambda} R_{s_\kappa}}{4\pi \left|\frac{(\beta_2(f_\kappa)+\beta_2(f_\lambda))}{2}(f_\kappa - f_\lambda)\right|}. \quad (29)$$

(29) is based on an approximation that is verified and has been validated in this work for all the XC terms and all the CUTs. In order to extend the approximation to the SC term, $\kappa = \lambda$, further analysis are required and in this study we use an SC estimator equivalent to the GGN implementation.

This solution enables accurate and fast NLI computation, and scales properly with the number of CUTs and interfering channels, providing a result for the investigated wideband transmission scenario in a computational time adequate for streaming operations.

V. SPLIT-STEP FOURIER METHOD SIMULATIONS

To validate the proposed methodology we have performed an SSFM simulation campaign using an internal simulation software environment, developed starting from [46]. The considered SSFM framework supports the simulation of a wideband transmission system using a simple description of the simulated spectrum, OLS, and receiver, by means of JSON files with syntax compliant with the GNPy library. The SSFM provides a numerical solution to (13), simulating the propagation of a WDM signal time series through successive position steps, dz.

The WDM signal at the fiber termination can be calculated by dividing the fiber length into consecutive segments, z_m, separated by a variable step, dz_m, as depicted in Fig. 7. If the step lengths are sufficiently small, the linear and nonlinear operator in (30) can be applied separately, with negligible inaccuracy [23], [47], obtaining the following the operator notation:

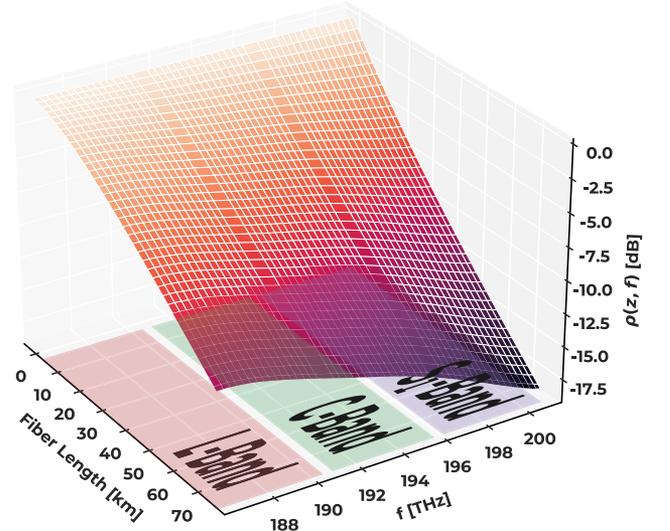$$\vec{A}(z_m + dz_m, t) \approx e^{\mathcal{L} dz_m} e^{\mathcal{N} dz_m} \vec{A}(z_m, t), \quad (30)$$

where the linear operator $\mathcal{L}$ can be effieicntly applied in the frequency domain by means of the fast Fourier transform (FFT) algorithm.

Moreover, the step lengths can be optimized in order to find a trade-off between simulation accuracy and computational cost, as shorter steps implies more accuracy, but also more Fourier transform evaluations, which are the most computationally expensive steps in the SSFM algorithm. In this work, we adopt the FWM-CLE step length optimization algorithm [47], which ensures that the simulation error remains constant as the simulation bandwidth is enlarged (we have set the accuracy parameter Φ_{FWM} to 0.01 rad for single channel simulations and to 1 rad otherwise).

Starting from $z_0 = 0$, for each step the SSFM algorithm first applies the nonlinear operator in the time domain, expressed as follows:

$$\vec{A}_N(z_m + dz_m, t) = \mathcal{F}^{-1}[\vec{A}(z_m, f)] \cdot e^{\iota \frac{8}{9}\tilde{\gamma}|\vec{A}(z_m,t)|^2 dz_m} .$$

where $\mathcal{F}$ stands for the Fourier transform applied using the FFT. The linear step is then applied to $\vec{A}_N(z_m + dz_m, t)$, obtaining the following evaluation of the WDM signal at the end of the m-th fiber step, in the frequency domain:

$$\vec{A}(z_m + dz_m, f) = \mathcal{F}[\vec{A}_N(z_m + dz_m, t)]$$
$$\cdot e^{-\iota\beta(f)dz_m} \frac{\rho(z_m + dz_m, f)}{\rho(z_m, f)},$$

where the exponential accounts for the dispersion accumulated along the length dz_m; the dispersion coefficient values for each frequency, $\beta(f)$, are interpolated along the simulated signal bandwidth using the measured curves of Fig. 3, and $\rho(z, f)$ is obtained by interpolating the solution of (21) for every considered frequency and position, as shown in Fig. 8. In particular, the solution of (21) has been evaluated with a fast SRS solver implementation available in GNPy considering the launch power
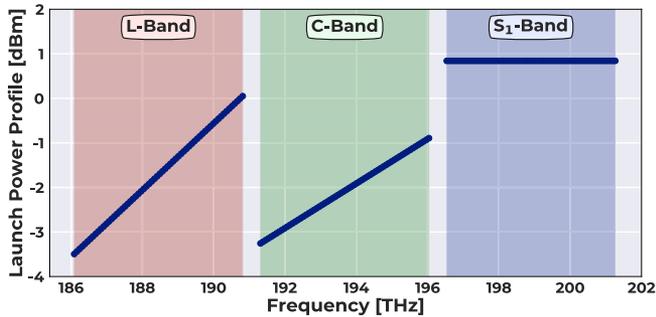
Fig. 9.   Launch power profile with average of -1.72, -2.07 and 0.84 dBm and tilts of 0.75, 0.50 and 0.0 dB/THz for L-, C- and S_1-bands, respectively.

profile shown in Fig. 9. This launch power profile has been obtained optimizing the GSNR average and flatness, as described in Section II.

A. SSFM Simulation Campaign

In this work, a C+L+S_1 400 G transmission scenario over a periodic 10-span OLS has been investigated. Each band is populated with 64 square root-raised cosine shaped channels with roll-off values of 0.15 at $R_s = 64$ GBaud in a 75 GHz fixed grid, for a total of 192 channels. We utilize a modulation format of polarization multiplexed (PM)-16- quadrature amplitude modulation (QAM) for all the CUTs, delivering 400 Gbps per channel, according to the 400G$-$ZR+ standard. A guard-band of 500 GHz has been placed between the bands in order to avoid band-splitting filter penalties, which is required to perform separate amplification, as depicted in the simulation setup of Fig. 10. The channel central frequencies range between 186.0 and 201.3 THz, respectively, for a total spectral occupancy of 15.3 THz. The channel launch power profile has been optimized using a exhaustive search algorithm [4], as explained in Section II.

Concerning the OLS, we consider 10 amplified fiber spans composed of ITU-T G.652D standard single mode fiber (SSMF). All fiber spans are 75 km long and are characterized by the frequency-dependent physical layer parameters described in Section III. In order to isolate the nonlinear term of (1), the WDM signal is propagated assuming noiseless amplifiers during the SSFM simulation. At the OLS termination, the WDM signal enters the DSP-based coherent receiver. We assume an ideal analog-to-digital converter (ADC), and as such filter out the four quadratures/polarization components of each CUT by re-sampling the WDM signal at 2 samples per symbol. We then apply ideal dispersion compensation, exactly recovering the amount of dispersion accumulated by each CUT. The signal is then fed to the adaptive equalizer stage, which converges to the matched filter. The equalizer stage is based on a least mean square (LMS) algorithm with 42 taps and an adaptation coefficient of 10^{-4}. This large tap size is set to maximize equalizer performance and to allow detection of even small amounts of nonlinear noise in the very first span of the OLS.

Next, a carrier phase estimation (CPE) block recovers the non-linear phase noise, neglecting transmitter laser phase noise. The

phase recovery algorithm uses the knowledge of the transmitted symbols to recover the carrier phase by dynamically setting the CPE memory. The optimal memory value maximizes the circularity of the noise clouds around the transmitted symbol scattering diagram. It should be noted that the optimal CPE memory, obtained by considering only the NLI noise, may not coincide with the optimum of a real systems, where the presence of ASE noise, which is the dominant impairment, produces a further trade off. However, the CPE optimization is outside the scope of this work and the chosen optimal CPE memory ensures the most accurate simulation of the NLI noise introduced by the fiber propagation.

The signal-to-noise ratio is then calculated upon the decision signal at 1 sample per symbol after the CPE stage. As we consider noiseless amplifiers, the estimated signal-to-noise ratio coincides with the $SNR_{NL;\lambda}$. Moreover, assuming an ideal receiver, the transmitted symbol series can be subtracted from the decision signal and $P_{NLI;\lambda}$ can be evaluated as the variance of the residual signal.

B. Disaggregated SSFM Using Single-Channel and Pump-and-Probe Configurations

Simulating the reference full spectral load scenario is practically unfeasible due to the enormous computational costs associated to the simulation of a WDM signal that occupies ≥ 15 THz. Furthermore, this approach would not allow the investigation of NLI generation in a spectrally disaggregated fashion. Therefore, for each band we have selected 7 equally spaced CUTs and carried out two sets of simulations in order to isolate the NLI contributors (the SC and XC) for each, as outlined in Fig. 10:

- *Single-Channel Configuration:* we simulate the propagation of solely the CUT, λ, with the estimation after the DSP consequently accounting only for the SC NLI component.
- *Pump-and-Probe Configuration:* we simulate the propagation of the CUT (the probe), λ, and a single interfering channel (the pump), κ, with an incremental frequency distance, Δf, from the probe. In this case, the estimation after the DSP accounts only for the XC NLI component; the SC NLI component is kept negligible by setting the probe power to a sufficiently low value (-20 dBm; the obtained result is then re-scaled to the required CUT power).

For practical reasons, we simulate a subset of pump and probe scenarios, outlined in the bottom of Fig. 10; for each CUT, all pumps up to $\Delta f = \pm 500$ GHz have been evaluated, along with four pumps located at $\Delta f = \pm 1$ THz and $\Delta f = \pm 2$ THz. The CUTs are kept as PM-16-QAM modulated, whereas the pumps are modulated using a Gaussian distributed symbol sequence, which provides an upper bound to the NLI intensity generation [48]. Additionally, channels propagating through an OLS can be considered as Gaussian distributed if a sufficient amount of dispersion has been accumulated [45], [49]. The entire set of single-channel and pump-and-probe simulations is performed using the fiber gain/loss profile of the overall C+L+S_1 transmission scenario, including the Raman effect, shown in Fig. 8.
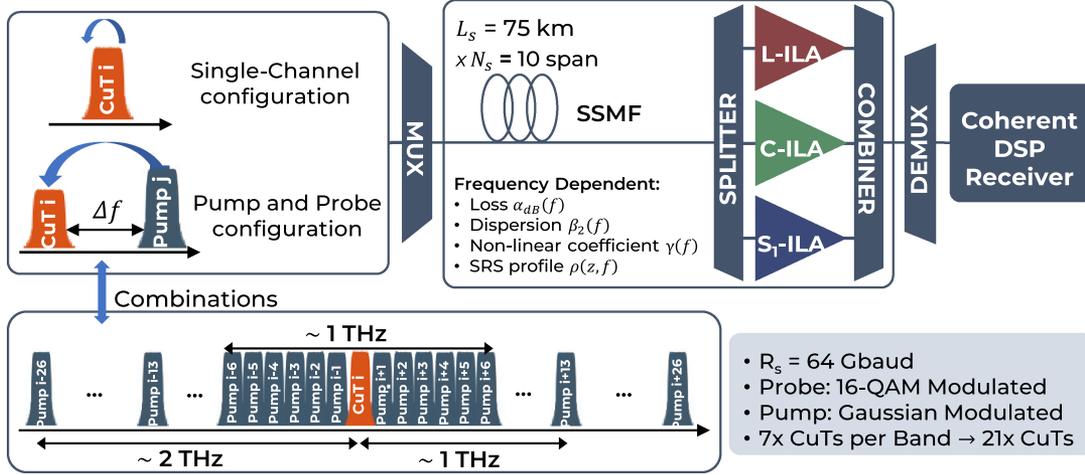
Fig. 10. A representation of the pump and probe campaign, simulated for each CUT. All pump and probe combinations within a 1 THz region encompassing the CUT, including a self-channel configuration, are propagated through the given line description and passed to the coherent DSP stage, along with additional pumps that lie 1 and 2 THz away from the CUT.

VI. RESULTS & ANALYSIS

We now present and compare the results of 10-span 400 G transmission through a C+L+S $_1$ OLS using the SSFM, GGN-based GNPy implementation, and the disaggregated approximate model proposed in this work. We first consider the separate contributions to the total $P_{\text{NLI};\lambda}^{(n)}$ at the n th span. As we consider a periodic OLS, $P_{\text{NLI};\lambda}^{(n)}$ can be normalized with respect to the launch power, obtaining:

$$\eta_{\lambda,\kappa}^{(n)} = \frac{P_{\text{NLI};\lambda}^{(n)}}{P_\lambda P_\kappa^2}, \qquad (31)$$

which represents the NLI efficiency when a single fiber span is considered, providing a direct metric for the frequency-dependent fiber parameter effects, and the separate NLI contributions of each interfering channel, κ.

In Fig. 11, we show $\eta_{\lambda,\kappa}^{(n)}$ evaluated at the OLS termination for the C-, L-, and S$_1$-band central channels, respectively. For all investigated CUTs, the GGN and proposed approximation provide a conservative estimation with respect to the interfering channel contribution given by the SSFM implementation. Furthermore, close to the CUT the SC and XC contributions of interfering channels are highly accurate for both methodologies, with inaccuracies increasing proportional to the frequency difference between the CUT and the interfering channel. In order to quantify the accuracy of the simulations we have presented in terms of overall QoT for each CUT, as a reference, we have extrapolated $\eta_{\lambda,\kappa}^{(n)}$ for all pump and probe configurations that have not been simulated using the SSFM, for each CUT; these extrapolations are shown with dashed lines in Fig. 11, and have been obtained applying the interpolation function defined in SciPy, a well-known open-source Python library, to the available $\eta_{\lambda,\kappa}^{(n)}$ simulations expressed in linear units. The SNR$_{\text{NL}}$ can now be evaluated by summing all distinct NLI contributions. The SNR$_{\text{NL}}$ comparisons between the extrapolated SSFM results, used as a reference in this analysis, the GGN-based GNPy

implementation and the proposed approximation are shown in Fig. 12(a) for all the CUTs. The GGN-based GNPy implementation and the proposed approximation provide an SNR$_{\text{NL}}$ prediction with average errors of 1.3 and 1.2 dB, respectively, and an equal maximum error of 1.7 dB. These inaccuracies are reduced by combining the simulated SNR$_{\text{NL}}$ values with the evaluated OSNR, as shown in Fig. 12(b), to find the GSNR for all implementations, shown in Fig. 12(c). With this QoT metric the two methodologies provide estimations with average errors of 0.3 and 0.2 dB, and maximum errors of 0.5 and 0.3, respectively. Considering these error margins, we remark that the proposed approximation provides a conservative, satisfactorily accurate and computationally fast result for all channels under test, and may reasonably be extended to larger bandwidths, given sufficient hardware and physical layer information.

In order to provide a reference value for the GSNR metrics, the results in Fig. 12(c) can be compared with the required minimum SNR threshold expressed in the OpenROADM 400 G 16-QAM transceiver specifications included in the GNPy equipment library. Such a device required a minimum SNR of 24 dB that is equivalent to a GSNR of 17 dB evaluated over the channel symbol rate, as the GSNR results presented in this work. Considering this threshold, both the GNPy GGN implementation and the proposed approximation provide an accurate prediction of the lightpath feasibility considering the SSFM extrapolation as the real scenario reference. In particular, both methodologies confirm the GSNR availability for the 400 G 16-QAM transmission over both the C- and L-band, whereas they predict that this transmission technology is unfeasible on the S$_1$-band, as it can be observed in Fig. 12(c). As a matter of fact, this analysis would be more complicated on a real scenario where additional penalties and inaccuracies of parameter values can affect the accuracy of the presented prediction. Nevertheless, QoT estimators as the GNPy GGN implementation have shown significant improvements in network planning, margin design and lightpath computation, gathering the interest of vendors and operators.
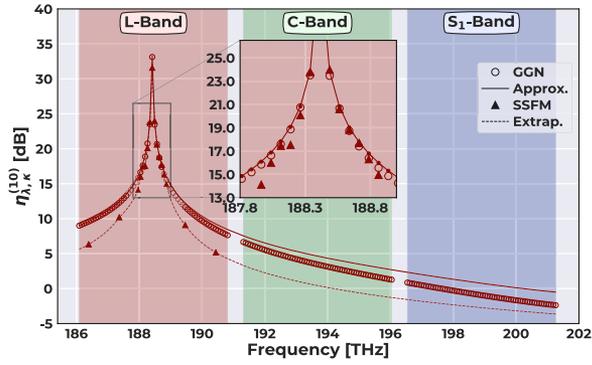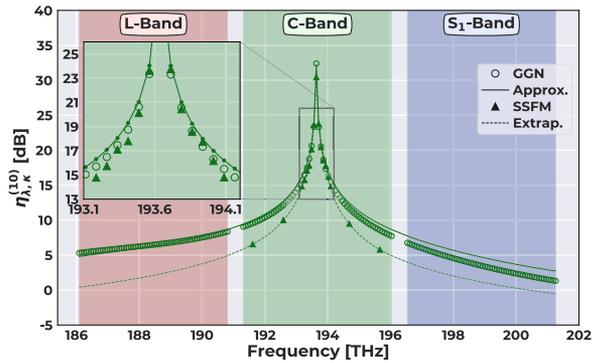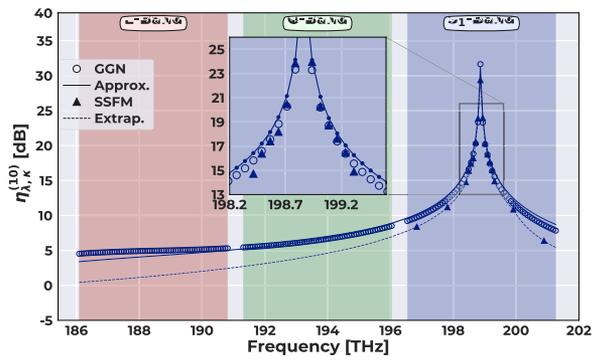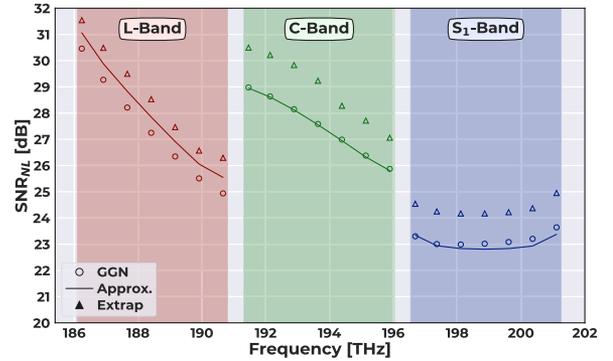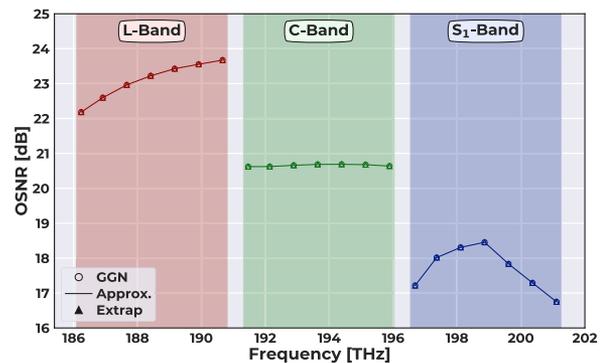
Fig. 11. Normalized NLI contribution for distinct pump and probe configurations at the OLS termination.

Fig. 12. SNR$_{NL}$, OSNR and GSNR comparison between the SSFM extrapolation, GGN-based GNPy implementation and the proposed approximation, for all CUTs.
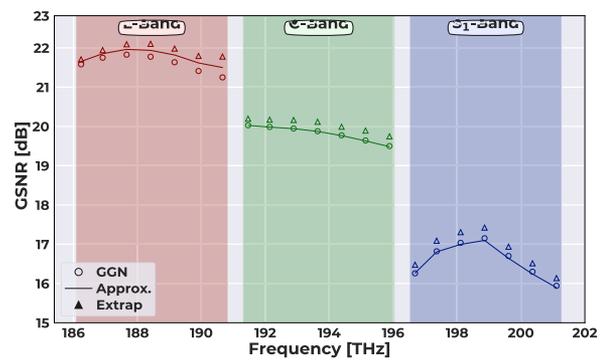
VII. CONCLUSION

In this work we have outlined the necessary frequency-dependent parameters which are required to accurately model multi-band/wideband optical network transmission beyond the C- and L-bands. We propose a scalable and disaggregated semi-analytical solution of the Manakov equation. Using a SSFM implementation which includes the frequency-dependent physical layer parameters, we validate the QoT predictions provided by the semi-analytical solution in a C+L+S$_1$ 400 G transmission scenario, along with a comparison with a GGN-based GNPy implementation. We demonstrate that this solution represents a valuable candidate for a multi-band/wideband optical network QoT estimator, given the achieved accuracy for the system under investigation and the limited computational complexity.

REFERENCES

[1] G. Wellbrock and T. J. Xia, "How will optical transport deal with future network traffic growth," in *Proc. Eur. Conf. Opt. Commun.*, 2014, pp. 1–3.

[2] J. K. Fischer *et al.*, "Maximizing the capacity of installed optical fiber infrastructure via wideband transmission," in *Proc. 20th Int. Conf. Transp. Opt. Netw.*, 2018, pp. 1–4.

[3] A. Ferrari *et al.*, "Assessment on the achievable throughput of multi-band ITU-T G.652.D fiber transmission systems," *J. Lightw. Technol.*, vol. 38, no. 16, pp. 4279–4291, Aug. 2020.

[4] B. Correia *et al.*, "Power control strategies and network performance assessment for C + L + S multiband optical transport," *J. Opt. Commun. Netw.*, vol. 13, no. 7, pp. 147–157, Jul. 2021.

[5] V. Lopez *et al.*, "Optimized design and challenges for C&L band optical line systems," *J. Lightw. Technol.*, vol. 38, no. 5, pp. 1080–1091, Mar. 2020.

[6] M. Cantono, R. Schmogrow, M. Newland, V. Vusirikala, and T. Hofmeister, "Opportunities and challenges of C + L transmission systems," *J. Lightw. Technol.*, vol. 38, no. 5, pp. 1050–1060, Mar. 2020.

[7] V. Curri and D. Calonico, "Multi-band and multi-service open optical networks: Applications and perspectives," in *Proc. 22nd Int. Conf. Transp. Opt. Netw.*, 2020, pp. 1–4.

[8] D. Semrau, E. Sillekens, P. Bayvel, and R. I. Killey, "Modeling and mitigation of fiber nonlinearity in wideband optical signal transmission," *J. Opt. Commun. Netw.*, vol. 12, no. 6, pp. C68–C76, 2020.

[9] C. Lasagni, P. Serena, and A. Bononi, "A Raman-aware enhanced GN-model to estimate the modulation format dependence of the SNR tilt in C + L band," in *Proc. 45th Eur. Conf. Opt. Commun.*, 2019, pp. 1–4.

[10] M. Cantono *et al.*, "On the interplay of nonlinear interference generation with stimulated Raman scattering for QoT estimation," *J. Lightw. Technol.*, vol. 36, no. 15, pp. 3131–3141, Aug. 2018.

[11] "GitHub repository of GNPy," [Online]. Available: https://github.com/Telecominfraproject/oopt-gnpy

[12] B. Correia *et al.*, "Networking performance of power optimized C + L + S multiband transmission," in *Proc. IEEE Glob. Commun. Conf.*, 2020, pp. 1–6.

[13] J. Kundrát, O. Havliš, J. Jedlinský, and J. Vojtěch, "Opening up ROADMs: Let us build a disaggregated open optical line system," *J. Lightw. Technol.*, vol. 37, no. 16, pp. 4041–4051, Aug. 2019.

[14] E. Riccardi, P. Gunning, Ó. G. de Dios, M. Quagliotti, V. López, and A. Lord, "An operator view on the introduction of white boxes into optical networks," *J. Lightw. Technol.*, vol. 36, no. 15, pp. 3062–3072, 2018.

[15] S. Gringeri, B. Basch, V. Shukla, R. Egorov, and T. J. Xia, "Flexible architectures for optical transport nodes and networks," *IEEE Commun. Mag.*, vol. 48, no. 7, pp. 40–50, Jul. 2010.

[16] V. Curri, "Software-defined WDM optical transport in disaggregated open optical networks," in *Proc. 22nd Int. Conf. Transp. Opt. Netw.*, 2020, pp. 1–4.

[17] M. Filer, M. Cantono, A. Ferrari, G. Grammel, G. Galimberti, and V. Curri, "Multi-vendor experimental validation of an open source QoT estimator for optical networks," *J. Lightw. Technol.*, vol. 36, no. 15, pp. 3073–3082, Aug. 2018.

[18] A. D'Amico *et al.*, "Experimental validation of GNPy in a multi-vendor flex-grid flex-rate WDM optical transport scenario," *J. Opt. Commun. Netw.*, vol. 14, no. 3, pp. 79–88, Mar. 2022. [Online]. Available: http://www.osapublishing.org/jocn/abstract.cfm?doi=10.1364/JOCN.442208

[19] A. D'Amico, E. London, E. Virgillito, A. Napoli, and V. Curri, "Inter-band GSNR degradations and leading impairments in C + L band 400G transmission," in *Proc. Int. Conf. Opt. Netw. Des. Model.*, 2021, pp. 1–3.

[20] E. Virgillito, E. London, A. D'Amico, B. Correia, A. Napoli, and V. Curri, "Single- vs. multi-band optimized power control in C + L WDM 400G systems," in *Proc. Opt. Fiber Commun. Conf. Exhibit.*, 2021, pp. 1–3.

[21] C. Lasagni, P. Serena, and A. Bononi, "Modeling nonlinear interference with sparse Raman-tilt equalization," *J. Lightw. Technol.*, vol. 39, no. 15, pp. 4980–4989, Aug. 2021.

[22] A. Napoli *et al.*, "Perspectives of multi-band optical communication systems," in *Proc. 23rd Opto-Electron. Commun. Conf.*, 2018, pp. 1–2.

[23] G. Agrawal, *Nonlinear Fiber Optics*, 5th ed. Boston, MA, USA: Academic, 2013.

[24] T. Li, *Optical Fiber Communications: Fiber Fabrication*. New York, NY, USA: Elsevier, 2012.

[25] S. Walker, "Rapid modeling and estimation of total spectral loss in optical fibers," *J. Lightw. Technol.*, vol. 4, no. 8, pp. 1125–1131, Aug. 1986.

[26] A. D'Amico *et al.*, "Enhancing lightpath QoT computation with machine learning in partially disaggregated optical networks," *IEEE Open J. Commun. Soc.*, vol. 2, pp. 564–574, Mar. 2021, doi: 10.1109/OJ-COMS.2021.3066913..

[27] G. Borraccini *et al.*, "Cognitive and autonomous QoT-driven optical line controller," *J. Opt. Commun. Netw.*, vol. 13, no. 10, pp. E23–E31, 2021.

[28] G. A. Thomas, B. I. Shraiman, P. F. Glodis, and M. J. Stephen, "Towards the clarity limit in optical fibre," *Nature*, vol. 404, no. 6775, pp. 262–264, 2000.

[29] J. Bromage, "Raman amplification for fiber communications systems," *J. Lightw. Technol.*, vol. 22, no. 1, pp. 79–93, Jan. 2004.

[30] E. Pincemin *et al.*, "Raman gain efficiencies of modern terrestrial transmission fibers in S-, C- and L-band," in *Proc. Nonlinear Guided Waves Appl.*, 2002, Art. no. NLTuC 2.

[31] K. Rottwitt, J. Bromage, A. J. Stentz, L. Leng, M. E. Lines, and H. Smith, "Scaling of the Raman gain coefficient: Applications to germanosilicate fibers," *J. Lightw. Technol.*, vol. 21, no. 7, pp. 1652–1662, Jul. 2003.

[32] "Amp-fl8221-sb-16 amplifier datasheet from fiberlabs inc," [Online]. Available: https://www.fiberlabs.com/bt_amp_index/s-band-bt-amp

[33] U. C. de Moura *et al.*, "Multi-band programmable gain Raman amplifier," *J. Lightw. Technol.*, vol. 39, no. 2, pp. 429–438, Jan. 2021.

[34] G. Borraccini *et al.*, "Autonomous Raman amplifiers in multi-band software-defined optical transport networks," *J. Opt. Commun. Netw.*, vol. 13, no. 10, pp. E53–E62, 2021.

[35] A. Mahajan, K. Christodoulopoulos, R. Martínez, S. Spadaro, and R. Muñoz, "Modeling EDFA gain ripple and filter penalties with machine learning for accurate QoT estimation," *J. Lightw. Technol.*, vol. 38, no. 9, pp. 2616–2629, May 2020.

[36] E. Virgillito, A. D'Amico, A. Ferrari, and V. Curri, "Observing and modeling wideband generation of non-linear interference," in *Proc. 21st Int. Conf. Transp. Opt. Netw.*, 2019, pp. 1–4.

[37] E. London, E. Virgillito, A. D'Amico, A. Napoli, and V. Curri, "Simulative assessment of non-linear interference generation within disaggregated optical line systems," *OSA Continuum*, vol. 3, no. 12, pp. 3378–3389, 2020.

[38] A. D'Amico, E. London, E. Virgillito, A. Napoli, and V. Curri, "Quality of transmission estimation for planning of disaggregated optical networks," in *Proc. Int. Conf. Opt. Netw. Des. Model.*, 2020, pp. 1–3.

[39] A. D'Amico *et al.*, "Using machine learning in an open optical line system controller," *J. Opt. Commun. Netw.*, vol. 12, no. 6, pp. C1–C11, 2020.

[40] A. D'Amico *et al.*, "GNPy experimental validation on flex-grid, flex-rate WDM optical transport scenarios," in *Proc. Opt. Fiber Commun. Conf.*, 2021, Art. no. W1G.2. [Online]. Available: http://www.osapublishing.org/abstract.cfm?URI=OFC-2021-W1G.2

[41] A. Ferrari *et al.*, "GNPy: An open source application for physical layer aware open optical networks," *IEEE/OSA J. Opt. Commun. Netw.*, vol. 12, no. 6, pp. C31–C40, Mar. 2020.

[42] C. R. Menyuk and B. S. Marks, "Interaction of polarization mode dispersion and nonlinearity in optical fiber transmission systems," *J. Lightw. Technol.*, vol. 24, no. 7, pp. 2806–2826, Jul. 2006. [Online]. Available: http://jlt.osa.org/abstract.cfm?URI=jlt-24-7-2806

[43] D. Pilori, M. Cantono, A. Ferrari, A. Carena, and V. Curri, "Observing the effect of polarization mode dispersion on nonlinear interference generation in wide-band optical links," *OSA Continuum*, vol. 2, no. 10, pp. 2856–2863, Oct. 2019. [Online]. Available: http://www.osapublishing.org/osac/abstract.cfm?URI=osac-2-10-2856

[44] S. Tariq and J. Palais, "A computer model of non-dispersion-limited stimulated Raman scattering in optical fiber multiple-channel communications," *J. Lightw. Technol.*, vol. 11, no. 12, pp. 1914–1924, 1993.

[45] P. Poggiolini *et al.*, "The GN-model of fiber non-linear propagation and its applications," *J. Lightw. Technol.*, vol. 32, no. 4, pp. 694–721, Feb. 2014.

[46] D. Pilori, M. Cantono, A. Carena, and V. Curri, "FFSS: The fast fiber simulator software," in *Proc. 19th Int. Conf. Transp. Opt. Netw.*, 2017, pp. 1–4.

[47] S. Musetti, P. Serena, and A. Bononi, "On the accuracy of split-step Fourier simulations for wideband nonlinear optical communications," *J. Lightw. Technol.*, vol. 36, no. 23, pp. 5669–5677, Dec. 2018.

[48] E. London, E. Virgillito, A. D'Amico, A. Napoli, and V. Curri, "Observing cross-channel NLI generation in disaggregated optical line systems," in *Proc. Asia Commun. Photon. Conf.*, 2021.

[49] A. Carena, G. Bosco, V. Curri, P. Poggiolini, M. T. Taiba, and F. Forghieri, "Statistical characterization of PM-QPSK signals after propagation in uncompensated fiber links," in *Proc. 36th Eur. Conf. Exhibit. Opt. Commun.*, 2010, pp. 1–3.